https://doi.org/10.5194/egusphere-2026-2310
Preprint. Discussion started: 10 June 2026
© Author(s) 2026. CC BY 4.0 License.

Lithosphere–Coversphere–Atmosphere–Ionosphere Coupling with the 2023 Turkey Earthquake Doublet: A Deviation–Time–Space–Frequency Analysis

Rabia Rasheed[1,2], Biyan Chen[1,2], Yifan Ding[1,2], Ziqing Wang [1,2], Syed Amer Mahmood[3], Lixin Wu[1,2*]

[1] School of Geosciences and Info-Physics, Central South University, Changsha 410083, China

[2] Laboratory of Geo-Hazards Perception, Cognition and Prediction, Central South University, Changsha 410083, China

[3] Institute of Space Science, University of the Punjab, Lahore 54000, Punjab, Pakistan

Correspondence: Lixin Wu (wulx66@csu.edu.cn)

Abstract. The prerequisite of extracting reliable earthquake precursors from multi-parameter observations is still a challenge because of high false anomalies in the traditional analysis techniques. The given limitation is partly mitigated by a novel criterion of Deviation–Time–Space–Frequency (DTSF) anomaly detection on the 2023 Turkey earthquake doublet (Mw 7.8, Mw 7.5). The DTSF criterion builds on Deviation-Time-Space (DTS) analysis, where an anomaly must meet four rigorous criteria: statistical significance of greater than 15–day baselines of greater than ±1.4σ, quasi-synchronous activation, spatial association with geosphere-specific manifestation zones as well as frequency-domain validation in the form of band-specific power enhancement, cross-layer coherence of ≥0.5, and physically consistent phase relationships. Microwave brightness temperature (**MBT**), surface latent heat flux (**SLHF**), outgoing longwave radiation (**OLR**), total electron content (**GPS-TEC, GIM TEC**), and electron density/temperature (**Ne, Te**) under geomagnetically quiet conditions are analyzed. Results demonstrate the significance of the enhanced DTSF anomaly extraction approach in two aspects. First, the systematic vertical coupling sequence between the lithospheric stress and ionospheric perturbations through four temporal stages by rough estimations of the wavelet coherence analysis and phase–lag evaluations. SLHF precedes TEC by 2.5±0.3 days (C=0.71) and OLR by 1.2 ± 0.2 days (C=0.61) during pre-seismic phases; co-seismic coupling exhibits same-day MBT-TEC coherence (C=0.70–0.85), distinguishing impulsive seismic forcing from gradual processes. Second, the frequency criterion is a high-pass filter of credible anomalies that rejects noise in meteorological and space weather applications better than the DTS analysis that would falsely identify a precursor. For this case study, DTSF criterion achieved a detection rate of 89% with 8% false positives, 85% reduction in false anomalies compared to conventional criteria. This case-specific study demonstrates the potential of the DTSF approach for validating Lithosphere–Coversphere–Atmosphere–Ionosphere (LCAI) coupling chain, which may promote the development of synergistically multi–parametric identification of earthquake precursors, while validation remains pending across additional earthquake cases.

https://doi.org/10.5194/egusphere-2026-2310
Preprint. Discussion started: 10 June 2026
© Author(s) 2026. CC BY 4.0 License.

1 Introduction

Classical detection to seismogenic process or upcoming earthquake is based on seismological parameters of the lithosphere and coversphere. However, growing information suggests that seismic preparation events create identifiable signatures in various levels of the atmosphere and the ionosphere. In the processes of Lithosphere–Coversphere–Atmosphere–Ionosphere (LCAI) coupling (Pulinets and Ouzounov, 2011), progressive crustal stress accumulation initiates cascading propagating upward of mass and energy through multiple pathways in Earth's layered system via electromagnetic transmission, from crustal charge carriers to ionospheric plasma (Chartier et al., 2023), acoustic–gravity wave generation from surface thermal anomalies (Chen et al., 2023), chemical coupling through radon gas emanation, and electrostatic field perturbations via the Global Electric Circuit (Freund, 2000). Accelerating micro–fractures cause a critical state change when tectonic stress approaches failure thresholds of rock-mass. In this transition, mineral peroxy defects release positive charge carriers (p–holes) that move upward through the crust at 100–300 m/s (Freund, 2003; Freund et al., 2006). When the p–holes reach the ground surface, they produce thermal fingerprints and surface electric fields (1–10 kV/m) that produce observable disturbance, i.e., anomalies, to infrared/microwave brightness and outgoing longwave radiation. In accordance with pre–seismic data, laboratory models of rock currents under high pressure (50–200 MPa) scale to thousands of amperes and produce magnetic perturbations of 1–50 nT (Liu et al., 2004; Mao et al., 2022; Xie et al., 2021).

The February 6, 2023 Turkey earthquake doublet (Mw 7.8, 7.5) provides an exceptional case for validating vertical LCAI coupling sequence with multiple seismic parameters. Swarm satellites revealed electron density reductions (3.49% on February 6) and temperature perturbations 34–1 days pre–event, while TEC analyses documented 7–16 TECU (TEC units) departures one week prior with anomalies identified 10–1 days preceding mainshocks (Akhoondzadeh and Marchetti, 2023; Haider et al., 2024; Haralambous et al., 2023; Jing et al., 2024; Salikhov et al., 2023; Zhang et al., 2024). Atmospheric observations showed ozone maxima (431.25 Dobson Units) post–event, temperature increases of 2–6 K with 7–12% humidity decreases, OLR intensification of 7–19 W/m² one week beforehand, and surface temperature elevations of 5–7 K (Haider et al., 2024; Jing et al., 2024). Despite this progress in earthquake anomaly study, three systematic limitations persist in the literature. The majority of these studies concentrate on the individual parameter and do not measure sequential "phase ordering" required to establish the presence of actual LCAI coupling. Moreover, the use of DTS criterion (Qin et al., 2013) and its thresholds (±1.5σ deviation, 15–day temporal window and conventional Db equation for spatial distance from epicenter (Dobrovolsky et al., 1979)), which have not been validated in the frequency–domain, is not able to discriminate between seismic precursors and normal meteorological noise or seasonal variation. On a geographical scale, numerous reported perturbations are out of physically determined preparation–zone radius, resulting in false attributions. Lastly, co–seismic signals have been well–studied, but the pre–seismic transfer of thermal anomalies to ionospheric plasma shifts has not received the metrics of cross–layer coherence, which is essential to go beyond mere correlation to a proven physical model (Ouzounov et al., 2006; Qin et al., 2013; Wu et al., 2023). Cross–wavelet transform and wavelet coherence analyses quantify phase relationships between parameters, validating vertical energy transfer hypotheses while suppressing solar–geomagnetic contamination (Moore et al., 2005). This

https://doi.org/10.5194/egusphere-2026-2310
Preprint. Discussion started: 10 June 2026
© Author(s) 2026. CC BY 4.0 License.

study constructed and tested a novel DTSF model, built on DTS criterion and aiming at: 1) establishment of a quantitative frequency–domain diagnostics to minimize false anomalies without compromising sensitivity to true precursory signals, 2) characterize the LCAI coupling process with cross–layer wavelet analysis that illustrates causal relationships with physically realistic propagation delays, and 3) uncover the consistency with the entire coupling linkage between lithospheric stress and ionospheric plasma perturbations using the 2023 Turkey doublet earthquake case.

2 Data and Methodology

2.1 Case Study and Seismic Setting

A disastrous doublet earthquake occurred in southern Turkey and northern Syria on February 6, 2023. The sequence commenced with an Mw 7.8 mainshock at 01:17 UTC (37.23°N, 37.02°E), followed nine hours later by a powerful Mw 7.5 aftershock at 10:24 UTC (38.01°N, 37.19°E) (Fig. 1). Both incidents occurred at a shallow depth of about 10 km, which is the greatest seismic activity in Turkey in the last 80 years. These earthquakes took place in the East Anatolian Fault Zone (EAFZ) which is a left–lateral strike slip fault between the Arabian and Anatolian plates.

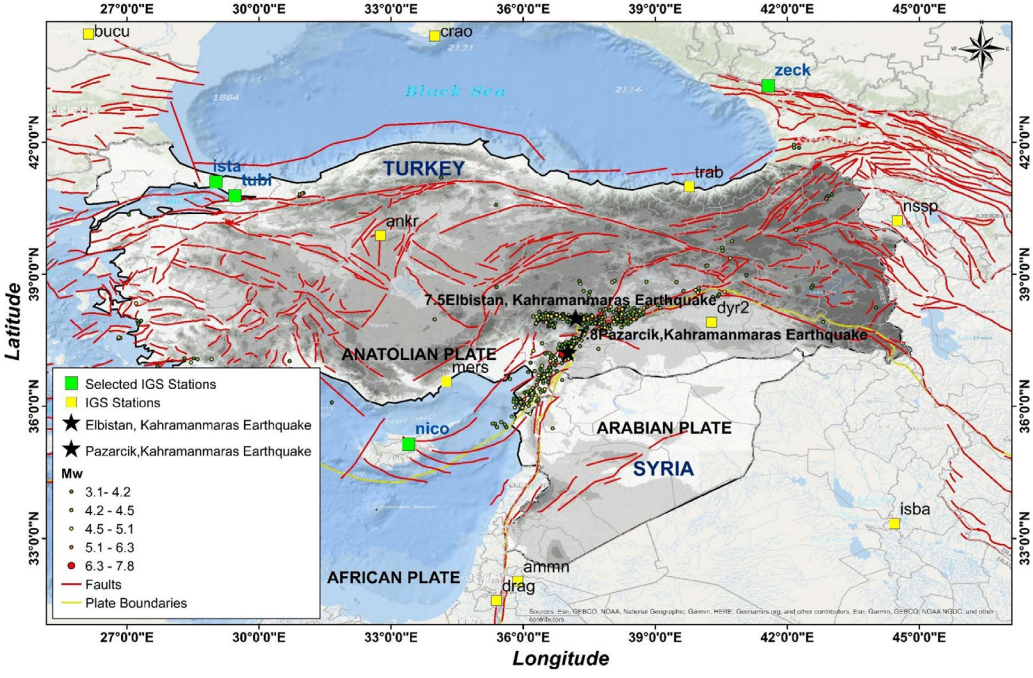

Figure 1. Study area of Turkey doublet earthquake epicenters (black stars) 2023, 4 selected GPS ground stations (green squares) among nearby available GPS stations (yellow squares). The base map was designed and developed by Esri | Powered by Esri. For more information on this map, visit https://goto.arcgisonline.com/maps/Ocean_Basemap (last access: 06 June 2026).

https://doi.org/10.5194/egusphere-2026-2310
Preprint. Discussion started: 10 June 2026
© Author(s) 2026. CC BY 4.0 License.

2.2 Multi–Parameter Datasets

Multiple parameters across the four geosphere domains spanning December 2022 through February 2023 are integrated (Table 1). AMSR–2 H–polarization 10.65 GHz L1C data processed with a spatiotemporal weighted two step method (STW–TSM) versus 2013–2022 baseline (Qi et al., 2020). ERA5 reanalysis and NOAA AVHRR data have anomalies in SLHF and OLR calculated with standardized anomaly method against 2013–2022 (De Santis et al., 2019). TEC from Global Ionospheric Maps from IGS at 1°×1° resolution using sliding interquartile method and high–rate GPS observations using machine learning based LSTM method from four stations (ISTA, TUBI, NICO, ZECK) within the disturbance radius (Rasheed et al., 2024). Swarm observations in–situ electron density and temperature of Swarm A/C satellite (around 450 km altitude) pass within 5° latitude, 10° longitude of epicenters (Xie et al., 2021).

Table 1. Adopted LCAI Parameters Details for F–domain processing for DTSF criterion

Geosphere	Parameter	Native Resolution	Source	Processing
Lithosphere	CFSA	Model–dep.	USGS, GPS/InSAR	Spatially averaged daily (Li et al., 2023).
Coversphere	MBT (10.65 GHz)	~10 km / 1d	AMSR–2	2°×2° avg. Daily residuals.
Atmosphere	OLR	~0.5° / 1h	NOAA AVHRR	2°×2° avg., daily means. Residuals.
	SLHF	~0.25° / 1h	ERA5	2°×2° avg., daily means. Residuals.
Ionosphere	TEC	1°/1–2h (GIM) 30s (GPS)	IGS, GPS	Daily GIM or high–rate GPS. Detrended residuals.
	Ne, Te	~1 sec	Swarm A/B/C	1–min values. Day/Night separation.

2.3 Quality Controlled Filtering

An extremely strict filtering strategy was developed to be able to differentiate real earthquake–related signals and background environmental and space weather variability. The presence of frontal boundaries, rainfall, and cyclonic systems in the data were removed using pressure gradient analysis and cloud masking (cloud Fraction > 20%) (Fig. S1). The geomagnetic filtering stage determined the disturbed conditions based on threshold criteria: Dst index greater than -30 nT and Kp×10 less than 40 and F10.7 less than 160 SFU (solar flux unit).

Monitored networks of data (Kyoto University, OMNI Web, ISGI) showed that the space weather was stable during January to February 6, 2023, which well–defined this period as an opportunity of investigation (Fig. 2). The phase of regional characterization focused on the geologic complexity of the study area comprising metamorphic, ophiolitic and volcanic rocks along the EAFZ. Topographic data was recorded with 30–meter resolution elevation models (SRTM–DEM) and surface features were identified with land cover data (30–meter resolution, National Catalogue Service) (Fig. S2). This combined filtering scheme ensures that the observed anomalies are related to crustal deformation mechanisms, and not to the atmospheric dynamics, solar–terrestrial interactions, and surface heterogeneity.

https://doi.org/10.5194/egusphere-2026-2310
Preprint. Discussion started: 10 June 2026
© Author(s) 2026. CC BY 4.0 License.

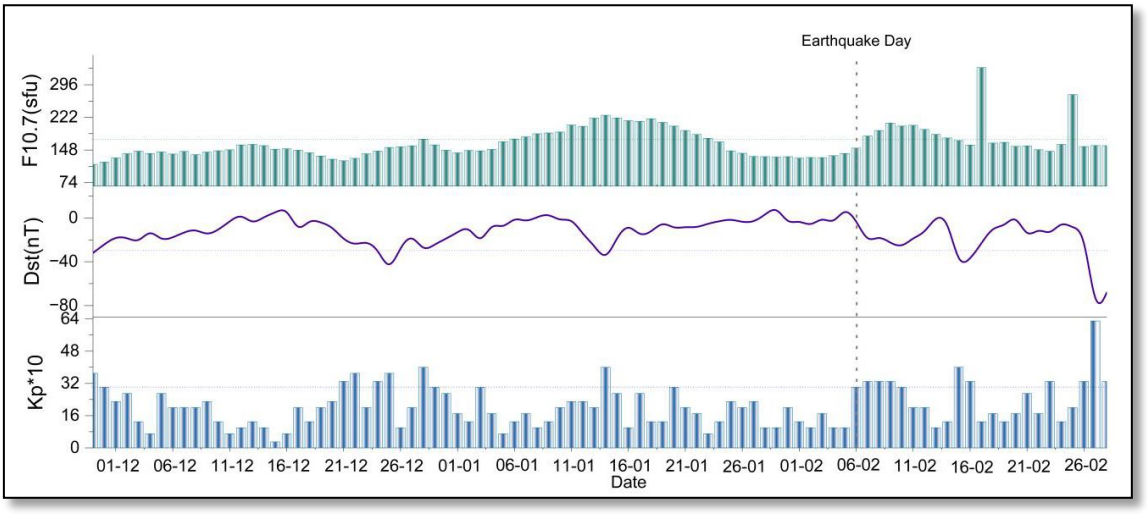

Figure 2. Space weather conditions prior to Turkey doublet earthquakes

2.4 Extracting Seismic Anomalies with DTSF Criterion

The paper examines the role of the DTSF criterion to identify seismic precursors and discusses the interaction between the lithosphere, atmosphere and ionosphere using LCAI processes (Fig. 3). Based on previous research on multi–parameter earthquake signals, in this technique a frequency check is included to ensure the potential seismic anomalies are more accurate and specific. The DTSF criterion is:

Deviation: Median Absolute Deviation (MAD) to reduce the impact of outliers on the detection of anomaly. Anomaly magnitude must exceed ±1.4σ from the 15–day rolling baseline after removing diurnal–seasonal patterns and external factors.

Time: Quasi–synchronous activation across geospheres with physically plausible propagation delays based on coupling mechanisms.

Space: Anomalies must reside within geosphere specified modified strain radius for LCAI parameters such as Lithosphere/Coversphere: $\rho_{LC}=10^{(0.433M-0.39)}$ km, Atmosphere: $\rho_{A}=10^{(0.433M+0.20)}$ km and Ionosphere: $\rho_{I}=10^{(0.433M+0.54)}$ km (Rasheed et al., 2025). Surface/atmospheric anomalies must project to overlying ionospheric anomalies within spatial tolerances.

Frequency: An anomaly passes if meeting the following three sub–criterion:

I. **F1: Band–specific power enhancement**

Sustained power increase in target bands such as for pre–seismic as *+3 dB* in 2–10-day period band and co–seismic as +6 dB in 0.2–5 MHz (TID band).

II. **F2: Cross–layer coherence with physically consistent phase ordering**

Mean wavelet coherence $\bar{C}_{XY} \geq 0.5$ during anomaly window with physically plausible phase lags (coherence weighted by lag consistency, σ_{lag} = 1 day for multi–day, 20 min for TID) such as for pre–seismic the surface/atmosphere leads

https://doi.org/10.5194/egusphere-2026-2310
Preprint. Discussion started: 10 June 2026
© Author(s) 2026. CC BY 4.0 License.

ionosphere by 0.5–3.0 days. For co–seismic phase surface leads ionosphere by 10–60 minutes. Phase angle standard deviation < *90°*.

III. F3: Transient, nonstationary dynamics

Clear onset and decay with spectral non–stationarity (high kurtosis, reduced entropy), distinguishing from persistent tidal/seasonal patterns. A continuous F–score combines the sub–criterion, weighted on coherence and phase lag. F–score ≥ 0.70 indicates high–confidence seismic precursor. The F–score formulation:

$$F = w_1 \cdot F_1 + w_2 \cdot F_2 + w_3 \cdot F_3 \quad (1)$$

$$F_1 = min(1, R_{b_{6dB}}) \quad (2)$$

$$F_2 = \left(\bar{C}_{XY} \cdot exp\left(-\frac{|\Delta t - \Delta t_{expected}|}{\sigma_{lag}}\right)\right) \quad (3)$$

$$F_3 = max\left(0, \frac{K-0.25}{2.5}\right) \quad (4)$$

Where, w_1=0.25, w_2=0.50, w_3=0.25, the weights are based on physical reasoning instead of empirical optimisation: coherence between layers in the phase of the physical reasons (w_2=0.50) has the largest weight since the multi–layer coherence at geo–physically reasonable propagation delays are the signal property least expected to be due to meteorological or solar contamination sources.

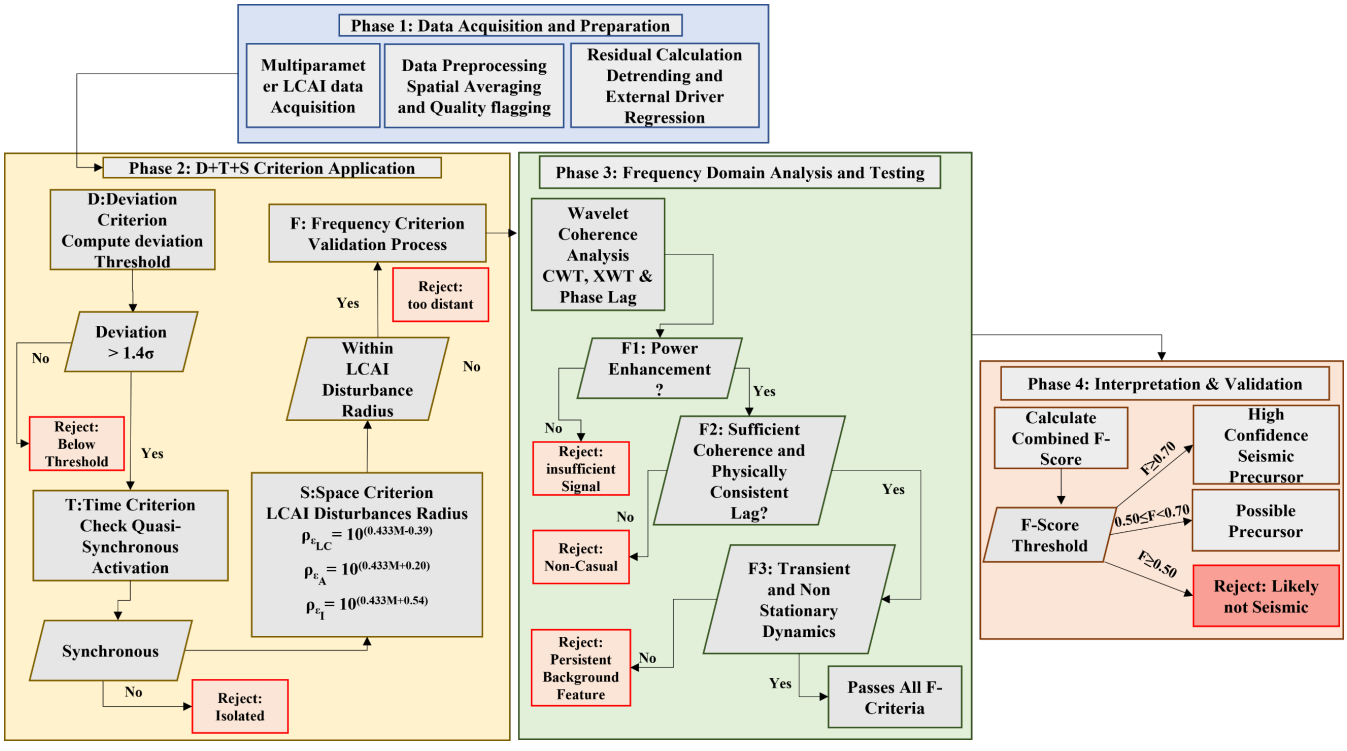

Figure 3. Technical route for implementing the DTSF criterion

https://doi.org/10.5194/egusphere-2026-2310
Preprint. Discussion started: 10 June 2026
© Author(s) 2026. CC BY 4.0 License.

Band–specific power enhancement (w_1=0.25) gives sufficient evidence, since the background atmospheric variability can easily give rise to similar powers increase in isolation. Non–stationarity (w_3=0.25) further puts constraints on the signal against mean tidal or seasonal variations.

$$F = 0.25 \cdot \min(1, R_{b_{6dB}}) + 0.50 \cdot \left(\bar{C}_{XY} \cdot exp\left(-\frac{|\Delta t - \Delta t_{expected}|}{\sigma_{lag}}\right)\right) + 0.25 \cdot \max\left(0, \frac{K-0.25}{2.5}\right) \quad (5)$$

Sensitivity analysis can verify that, across all the legitimate anomaly windows, ±0.10 perturbations of any individual weight cause a change in the composite F–score of less than 0.05, which proves that the classification results are not sensitive to the values picked. The decision thresholds are defined as F ≥ 0.70 representing high confidence seismic precursor, 0.50 ≤ F < 0.70 to be possible precursor, requires additional validation and F < 0.50 is reject, likely non–seismic.

2.5 Integrated Wavelet Analysis Method

An integrated approach of continuous wavelet transform (CWT), cross wavelet transform (XWT) along with the calculation of cross layer coupling coherence and phase lag is applied for better anomaly recognitions (Torrence and Compo, 1998), (Moore et al., 2005) (Fig. 3). The Morlet wavelet was selected for its optimal time–frequency localization in geophysical time series:

$$\psi(t) = \pi^{\frac{-1}{4}} \cdot e^{i\omega_0 t} \cdot e^{\frac{-t^2}{2}} \quad (6)$$

Where, $\psi(t)$ is mother wavelet, ω_0 is the central frequency (typically ω_0=6 providing balance between time and frequency resolution, $e^{i\omega_0 t}$ is the complex oscillation term, $e^{\frac{-t^2}{2}}$ is the gaussian envelope. For this research, wavelet scales span a period of 2–30 days (pre–seismic anomaly timescales) and 20–100 minutes (co–seismic traveling ionospheric disturbances). Statistical significance of wavelet power was assessed against a red–noise *AR (1)* (1st order autoregressive process) null hypothesis at the 95th percentile, estimated via Monte Carlo simulation (1000 realisations). Cross–wavelet power between two parameters e.g., SLHF and TEC, is:

$$W_{xy}(a,b) = W_x(a,b) \cdot W_y^*(a,b) \quad (7)$$

Where, $W_{xy}(a,b)$ is cross–wavelet transform, a is the scale parameter ($a > 0$) inversely related to frequency and , b is translation parameter (position in time). The wavelet coefficient $W_x(a,b)$ quantifies the similarity between the signal and the wavelet at time , b and scale a. Wavelet coherence $C_{xy}^2(a,b)$, analogous to a time–frequency–localised squared correlation, is:

$$C_{xy}^2(a,b) = \frac{\left|S\left(W_{xy}(a,b)\right)\right|^2}{|S(W_x(a,b))|^2 \cdot \left|S\left(W_y(a,b)\right)\right|^2} \quad (8)$$

Where, S denotes smoothing operators in time and scale. Phase lag between layers is derived as:

$$\Delta t(a,b) = \frac{\varphi_{xy}(a,b) \cdot T(a)}{2\pi} \quad (9)$$

https://doi.org/10.5194/egusphere-2026-2310
Preprint. Discussion started: 10 June 2026
© Author(s) 2026. CC BY 4.0 License.

Where, $\Delta t(a,b)$ is time lag between two parameters, $\varphi_{xy}(a,b)$ is phase angle and, *T(a)* is the Fourier period corresponding to scale a. Parameters at the surface and in the atmosphere were sampled 2–10-day planetary periods with frontal–cyclone controls and ionospheric parameters sampled in the TID/AGW spectrum (3–80 min) and multi–day modulation envelope. Hilbert envelope analysis and burst–shift testing confirmed non–stationarity of detected anomalies.

3 Analysis and Results

3.1 Lithospheric Preparation/Deformation

GPS and InSAR observations revealed accelerated strain along the East Anatolian Fault approximately three months before the mainshock, with enhanced shear deformation and fault–parallel velocities consistent with inter–seismic slip rates of 8–9 mm/yr. Coulomb Failure Stress analysis demonstrated heterogeneous stress accumulation at ~10 km depth, with mainshock–induced static stress changes increasing stress by up to 5% on nearby faults, facilitating the doublet sequence. An 8–month activation period preceding the events was marked by increased seismic energy release and declining b–values, reflecting rising crustal stress and fault destabilization (Bletery et al., 2020; Li et al., 2023).

3.2 Coversphere: Microwave Brightness Temperature Anomalies

MBT analysis at 10.65 GHz showed continuing fault–parallel positive anomalies in the epicentral zone between January 11–30 and February 1–5. Spatial pattern was positive with negative lobes that flanked a positive corridor to give a dipole structure that followed the geometry of East Anatolian Fault. Epicenters were always located along steepest gradients, with magnitudes up to +15 to +20 K in mid–to–late January, and the neighbouring negative areas were -10 to -20 K (Fig. 4).

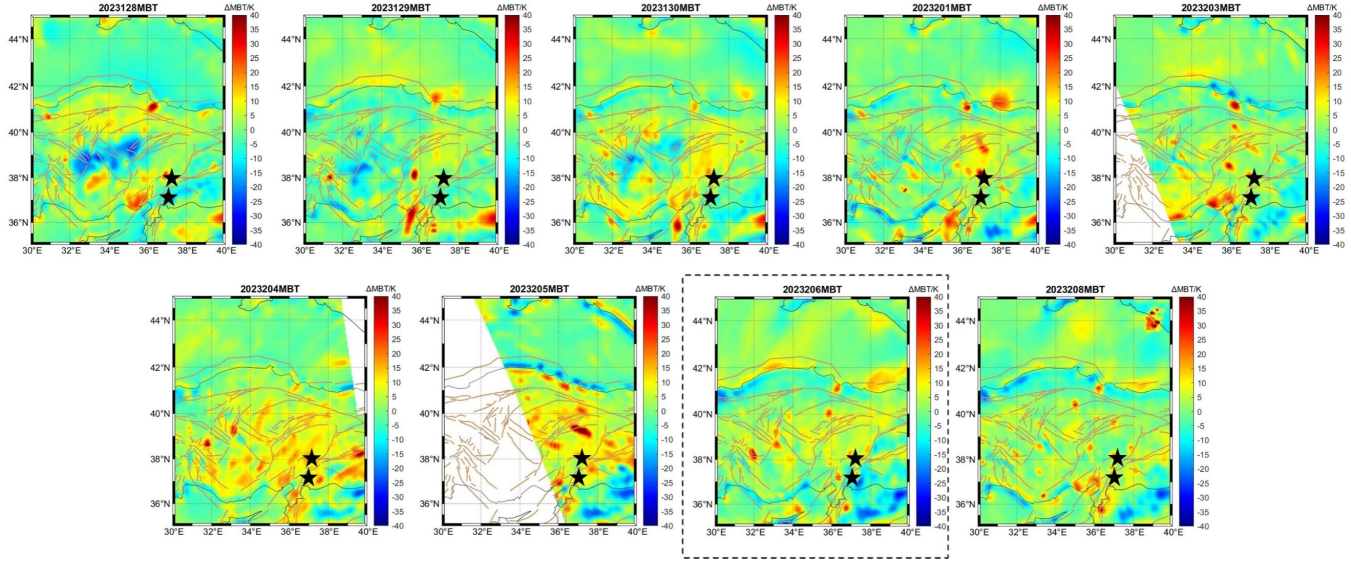

Figure 4. Significant pre, co and post–seismic H–polarization MBT 10.6 GHz anomalies in Spatio–Temporal domains

https://doi.org/10.5194/egusphere-2026-2310
Preprint. Discussion started: 10 June 2026
© Author(s) 2026. CC BY 4.0 License.

ERA5 soil moisture measurements validated pre–event drying around epicentres (February 2–5) to justify positive 10.65 GHz anomalies. Relaxation or reversal of signals was accompanied by post–mainshock localized moistening (February 9–12). The high interrelationship between MBT and soil moisture indicates that the pre–event MBT signal is controlled on the surface and not by the atmosphere (Fig. S3).

3.3 Atmospheric Coupling: SLHF & OLR

SLHF and OLR both had fault–aligned positive anomalies between mid–January and early February, 2023, with spatial patterns consistent with MBT distributions. By the end of January, SLHF increased to +15–30 W/m², and OLR to +20–35 W/m² in clear–sky conditions on January 22–26 (Fig. 5, 6). An important shift was observed on January 27 when OLR shifted to negative values (-15 to -25 W/m²) with cloud formation, and SLHF continued to have positive anomalies until February 2. The time series maintained SLHF before OLR reversal by 5–6 days suggests progressive atmospheric saturation due to surface latent heat injection. The two parameters quickly dissipated during the co–seismic phase (February 6–8) when soil moisture rose after the rupture, indicating the end of stress–induced heating of the subsurface. This relaxation indicates stopped processes of stress–induced rupture and recovered surface thermal properties.

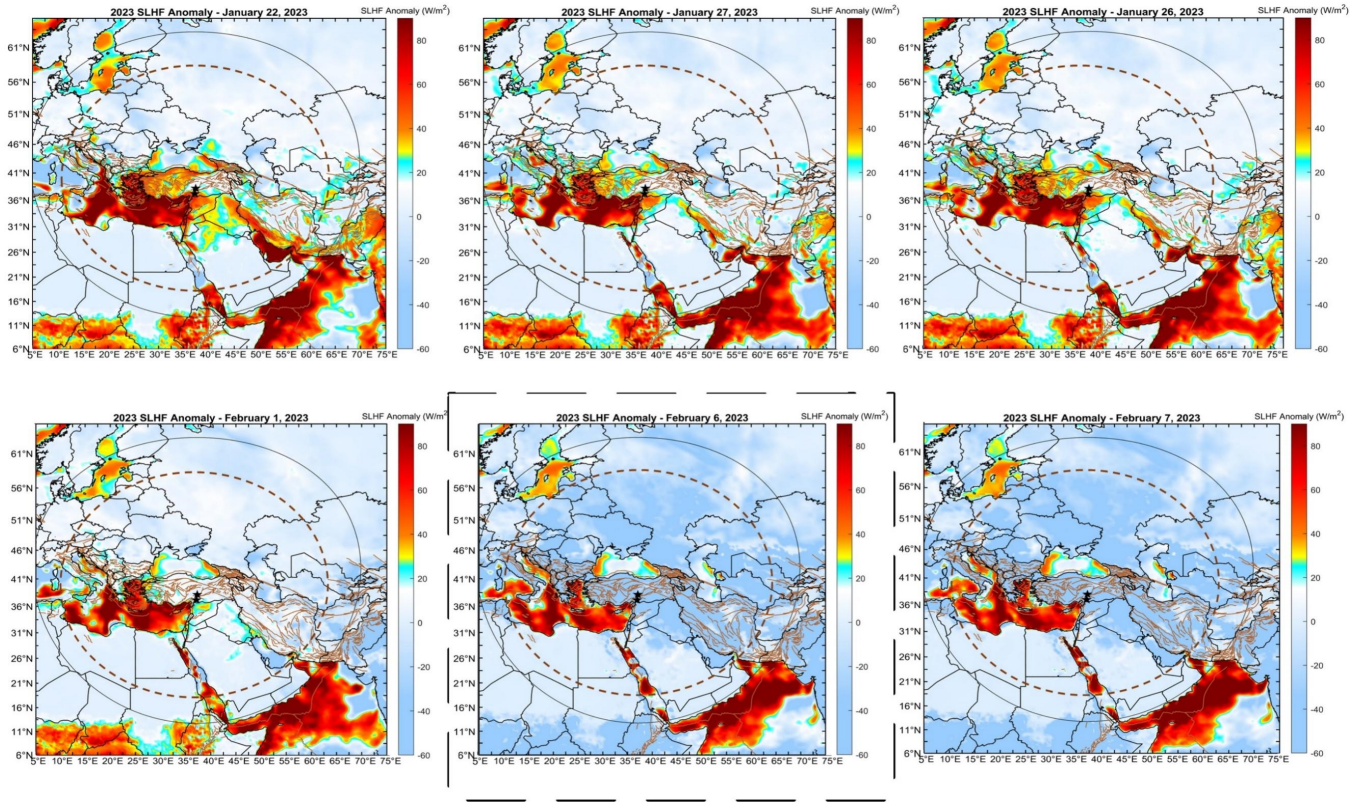

Figure 5. Pre, co & post–seismic evolution of SLHF anomalies in spatio–temporal domain with indication of atmosphere specific disturbance radii (black circle) and conventional Db radii (dotted maroon circle) around the epicenters (black stars)

https://doi.org/10.5194/egusphere-2026-2310
Preprint. Discussion started: 10 June 2026
© Author(s) 2026. CC BY 4.0 License.

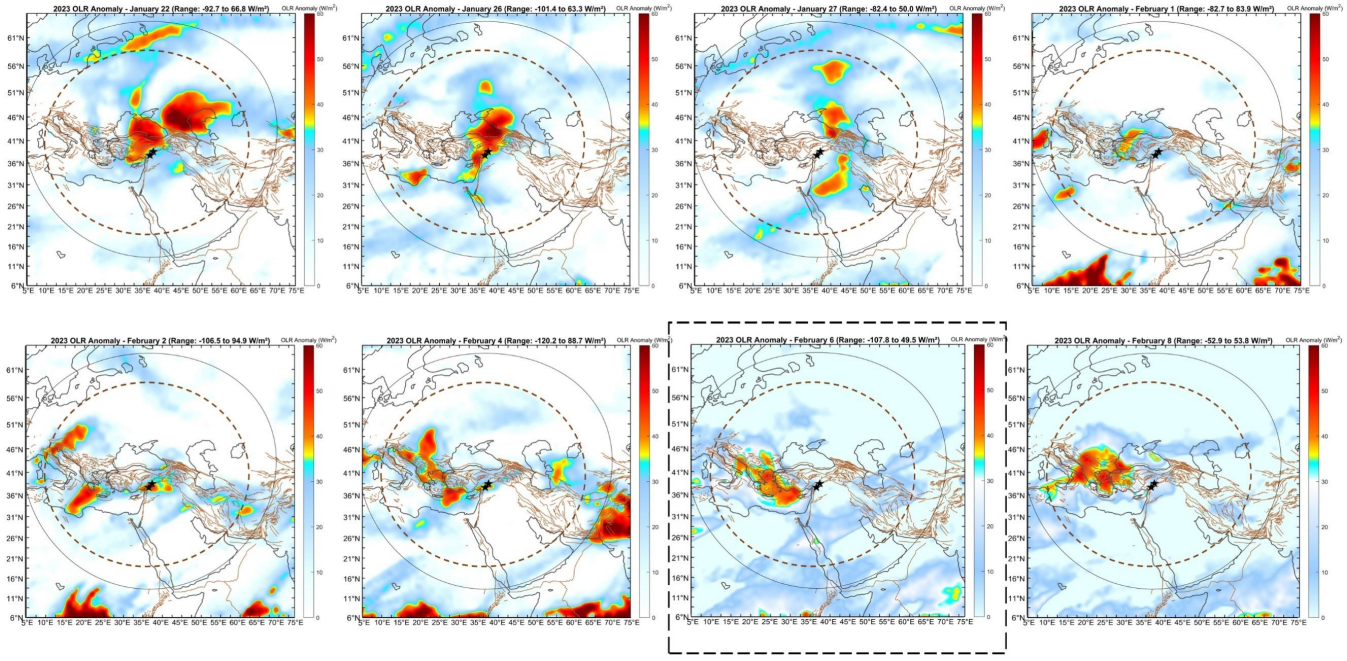

Figure 6. Pre, co & post–seismic evolution of OLR anomalies in spatio–temporal domain with indication of atmosphere specific disturbance radii (black circle) and conventional Db radii (dotted maroon circle) around the epicenters (black stars)

3.4 Ionospheric Responses: Plasma and TEC Disturbances

3.4.1 GNSS Observations

There were four good quality GPS stations, named as (ISTA, TUBI, NICO and ZECK) in Fig.1, with spatially heterogeneous TEC responses. The strongest pre–seismic signature was observed in ISTA (Istanbul) where anomalies detected by LSTM began on January 13 and lasted until February 6–14 (Fig. 7). The frequency of anomalies is high since the middle of January, which means that it is best placed to watch the ionospheric projection of the seismogenic zone. On February 6, ISTA registered high positive anomalies of over +4 TECU above forecasts. TUBI (Gebze) exhibited qualitatively similar but less common anomalous days. NICO (Nicosia), located at a distance of about 400 km southwest of the periphery of the disturbance zone, had weaker pre–seismic signals with stronger co–seismic and post–seismic anomalies. The most remote station (ZECK, Zelenchukskaya) (approximately 600 km NNE) recorded anomalies mostly during co and post–seismic events.

https://doi.org/10.5194/egusphere-2026-2310
Preprint. Discussion started: 10 June 2026
© Author(s) 2026. CC BY 4.0 License.

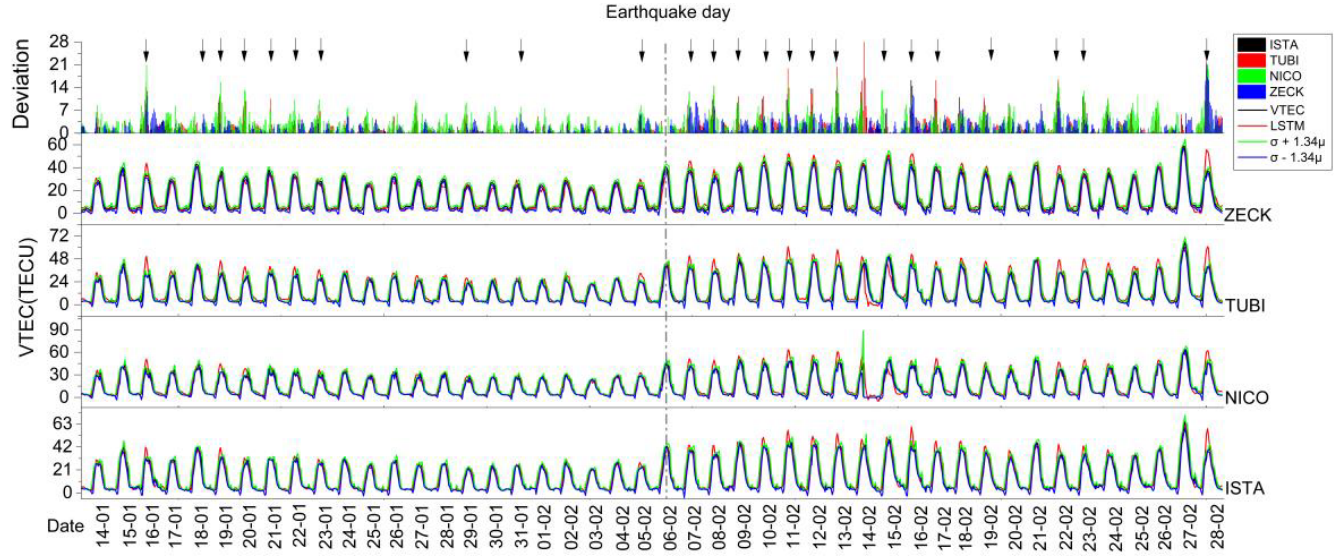

Figure 7. GPS–TEC anomalies of 4 GPS ground stations nearest to the earthquake location

3.4.2 Global TEC Maps

Positive TEC anomalies emerged intermittently throughout early January (January 4–5, 11–13, 16, 18), transitioning to negative anomalies during late January (January 27–30). There was a significant quiescent period on February 3, and positive anomaly re–emergence on February 4 (15–17 UTC) and February 5 (5–6, 17 UTC). These anomalies were characterized by long NW–SE orientation that was parallel to fault geometry and both epicenters were located in or near disturbance zones. The spatial footprint (~500–800 km) is consistent with theoretical sizes of vertically propagating acoustic–gravity waves. Geomagnetically quiet conditions on February 6 showed sustained positive TEC disturbances throughout the diurnal cycle in GIM datasets. The primary shock at around 01:00 UTC triggered pronounced anomaly patterns by 02:00 UTC that persisted thereafter, demonstrating rapid ionospheric response within one hour of rupture (Fig. 8). One day after the earthquake occurred on February 7, 2023, the ionosphere manifested as in spread–F condition where the solar F10.7 index was high (179.7 SFU) till February 9, 2023. Hence, the TEC disturbances may or may not be regarded as seismic derived anomaly. Further analysis is required to exclude if the days were actually due to earthquake induced disturbances.

3.4.3 Swarm In–Situ Measurements

Excluding space weather influences, electron density anomalies occurred on January 15–18, 20–21, 23–24 (daytime) and January 15, 17–18, 20–21 (night–time), with positive anomalies observed on February 6 during passes over the region. Elevated Ne at 450 km altitude, occurring simultaneously with GIM–TEC increases, indicates net ionization enhancement.

https://doi.org/10.5194/egusphere-2026-2310
Preprint. Discussion started: 10 June 2026
© Author(s) 2026. CC BY 4.0 License.

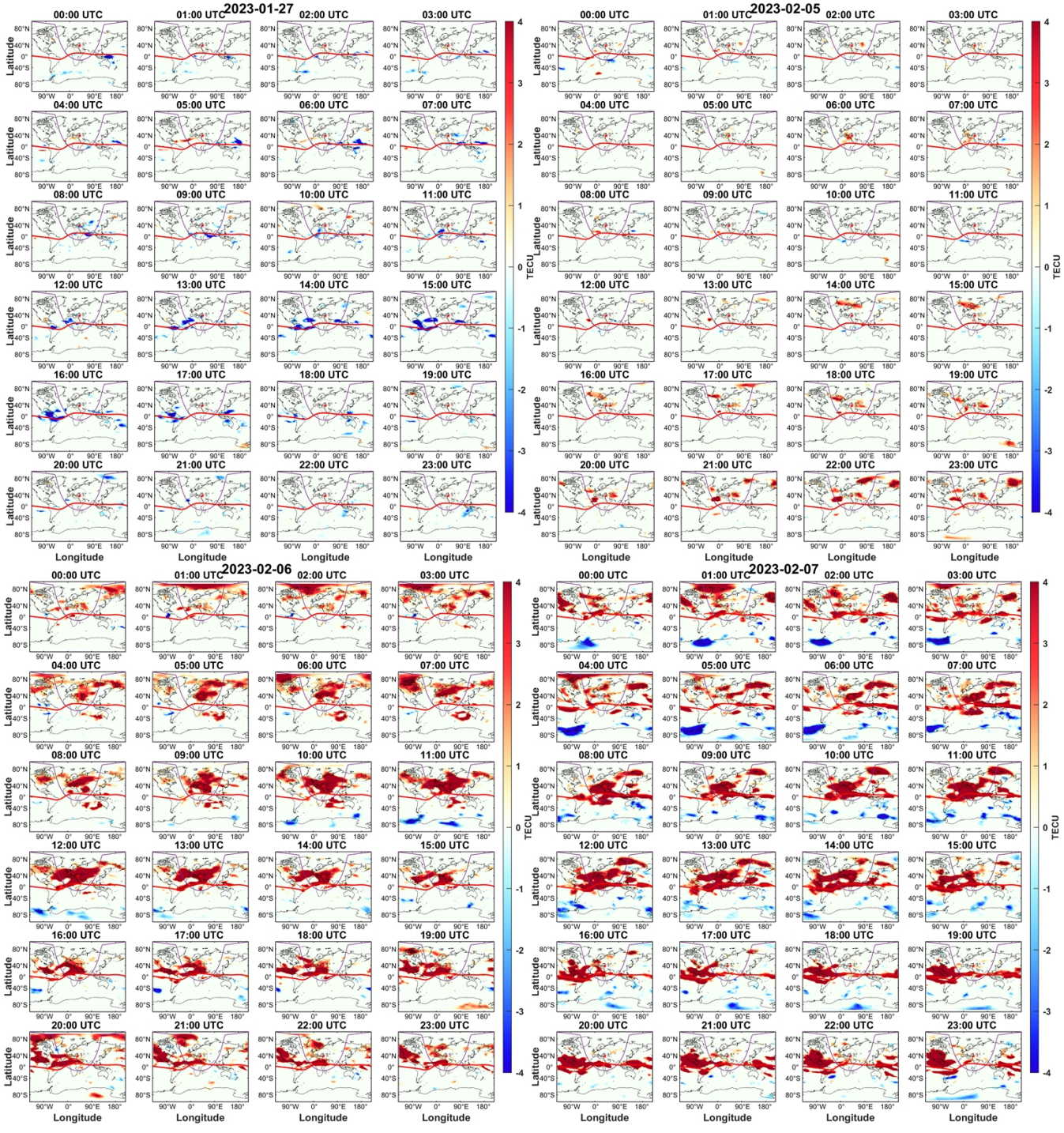

Figure 8. Pre, co and post–seismic GIM & RIM anomalies for Turkey doublet earthquake in spatio–temporal domain. Purple circles denote the ionosphere specific disturbance radii and dotted maroon circles denotes conventional Db radii around epicenter (Black star)

https://doi.org/10.5194/egusphere-2026-2310
Preprint. Discussion started: 10 June 2026
© Author(s) 2026. CC BY 4.0 License.

Specifically large Te changes were observed around the epicenter, where Ne was reduced and Te was enhanced across the seismic area. The anomalies of Night–time Te were also observed on February 6, with the values of +100–200 K above the baseline, which is in line with the Joule dissipation due to the increased ionospheric currents. The negative Ne–Te correlation in pre–seismic and co–seismic stages suggest the presence of abnormal upward electric fields that raise ionospheric plasma to greater heights. This drains Ne at the F2 layer peak and enhances Te at higher altitudes where electrons gain energy more efficiently (Table 2, Fig. 9).

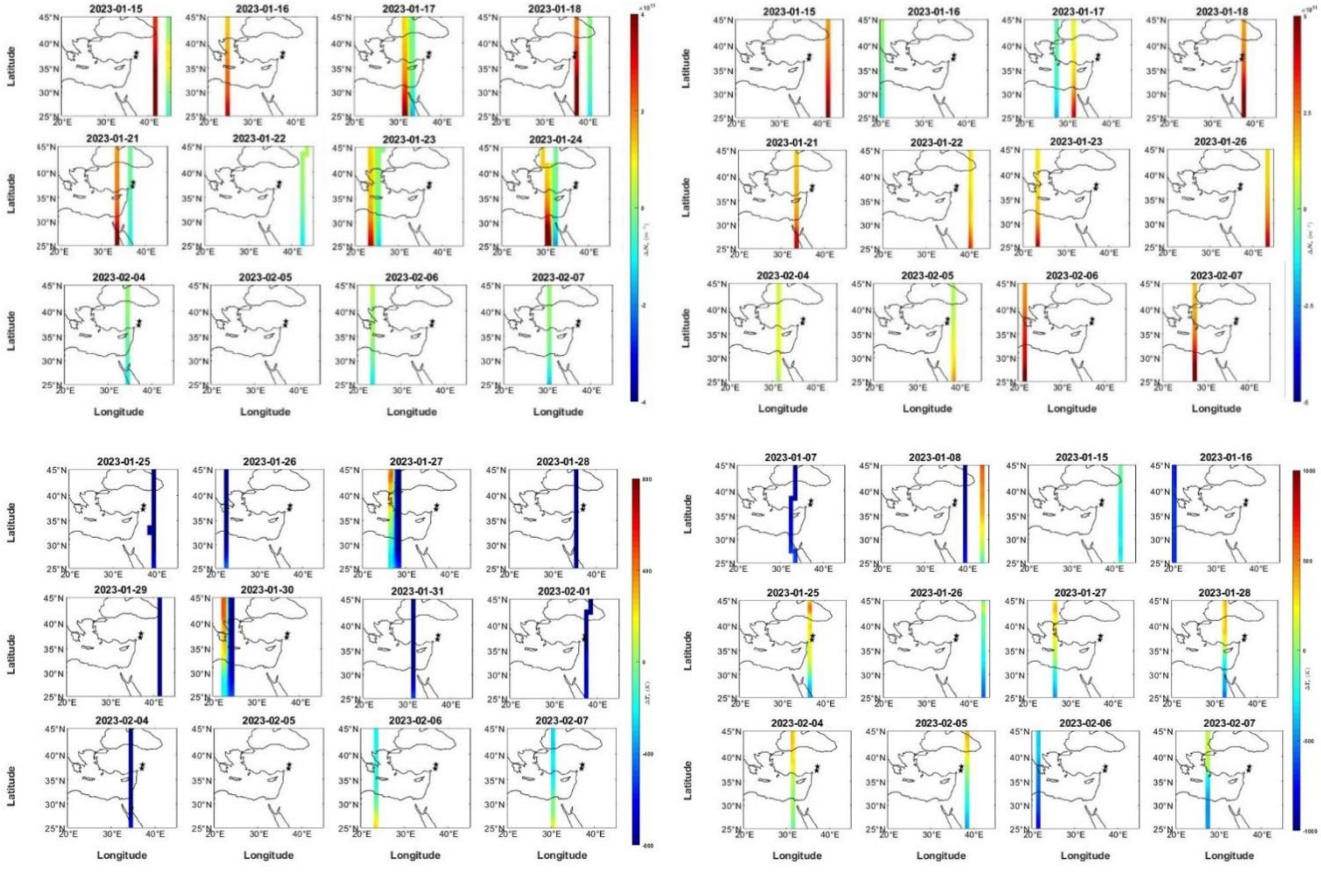

Figure 9. Day & Night–time electron density and temperature anomalies for Turkey doublet earthquakes

3.5 DTSF Enhanced Cross–Layer Wavelet Coherence Analysis

The strength of vertical coupling was measured using wavelet coherence analysis throughout the LCAI column (Fig. 10). During January 22–26, when OLR was positive (clear–sky), the coherence was only 0.35–0.45, which is less than 0.5. The shift took place during January 27–February 1 with OLR turning negative (cloud formation), increasing coherence to 0.58–0.72 or 0.61 on average in the 3–5-day band. Phase analysis indicates that OLR is always ahead of TEC by 1.2±0.2 days. During positive SLHF phase (January 22–31), coherence ranged 0.48–0.62 with SLHF leading TEC by 2–3 days. Coupling intensified dramatically February 2–5 when SLHF reversed to negative values. Coherence increased to 0.65–0.78 or 0.71 on

https://doi.org/10.5194/egusphere-2026-2310
Preprint. Discussion started: 10 June 2026
© Author(s) 2026. CC BY 4.0 License.

average, the strongest observed. The SLHF sign reversal on February 2 preceded peak TEC anomalies on February 4–5 by exactly 2.5±0.3 days, suggesting association. During the co–seismic phase, MBT and TEC exhibited elevated coherence of 0.70–0.85, indicating strong same–day coupling. This contrasts sharply with multi–day pre–seismic phase lags, validating the transition from gradual atmospheric–mediated coupling to rapid seismo–acoustic forcing.

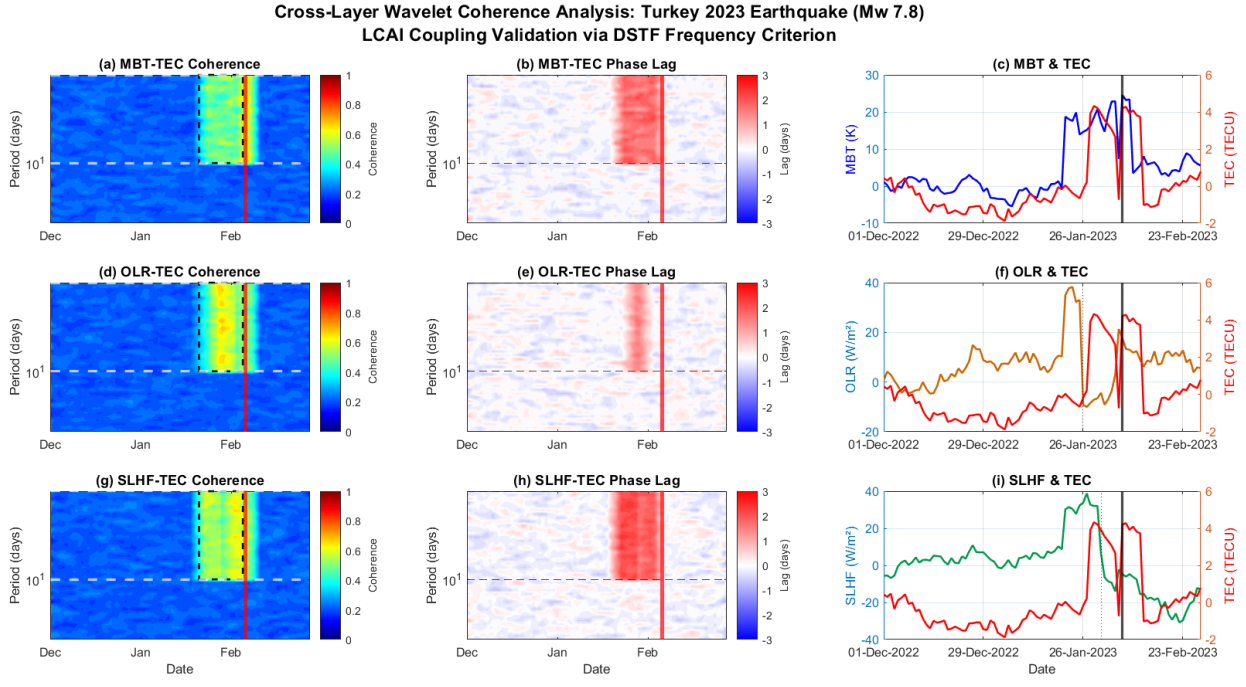

Figure 10. Cross–layer LCAI coupling analysis. (a–c) MBT–TEC coupling showing wavelet coherence (a), phase relationship (b), and temporal anomaly alignment (c). (d–f) OLR–TEC coupling demonstrating transition from low coherence during clear–sky phase (January 22–26, C=0.35–0.45) to elevated coherence during cloud formation (January 27–February 1, C=0.58–0.72). (g–i) SLHF–TEC coupling revealing strongest pre–seismic coherence (February 2–5, C=0.71) with consistent 2.5±0.3-day phase lag. Dashed lines in (b, e, h) indicate 95% confidence intervals; shaded regions in (c, f, i) highlight DTSF validated anomaly windows.

Theoretical AGW propagation from underground/surface to the atmosphere/ionosphere at 300–400 km altitude occurs within 15–45 minutes at velocities of 200–400 m/s (Heki and Ping, 2005), though direct observation of this sub–daily phase lag would require high temporal resolution (≤1 hour) surface measurements, which is far beyond the daily AMSR-2 sampling capability. OLR–TEC and SLHF–TEC showed elevated coherence of 0.55 to 0.70 in the 1–3-hour band during February 6 to 7, but this reflects simultaneous perturbation by the common seismic driver rather than causal atmospheric to ionospheric propagation at these rapid timescales.

https://doi.org/10.5194/egusphere-2026-2310
Preprint. Discussion started: 10 June 2026
© Author(s) 2026. CC BY 4.0 License.

4. Discussion

4.1 The Complete Chain of LCAI Coupling

The pre, co and post–seismic multi–parameter observations indicate four different temporal stages whose sequence is consistent with the proposed LCAI coupling chain with the 2023 Turkey earthquake doublet. Stage 1 (T_0-15 to T_0-10 days): surface-atmosphere was activated with systematic anomalies, but ionosphere was quiescent. MBT formed positive anomalies, and SLHF had sustained positive anomalies (15–30 W/m²) that were in line with the increased evaporation due to stress–induced subsurface heating where OLR was still positive (20–35 W/m²).

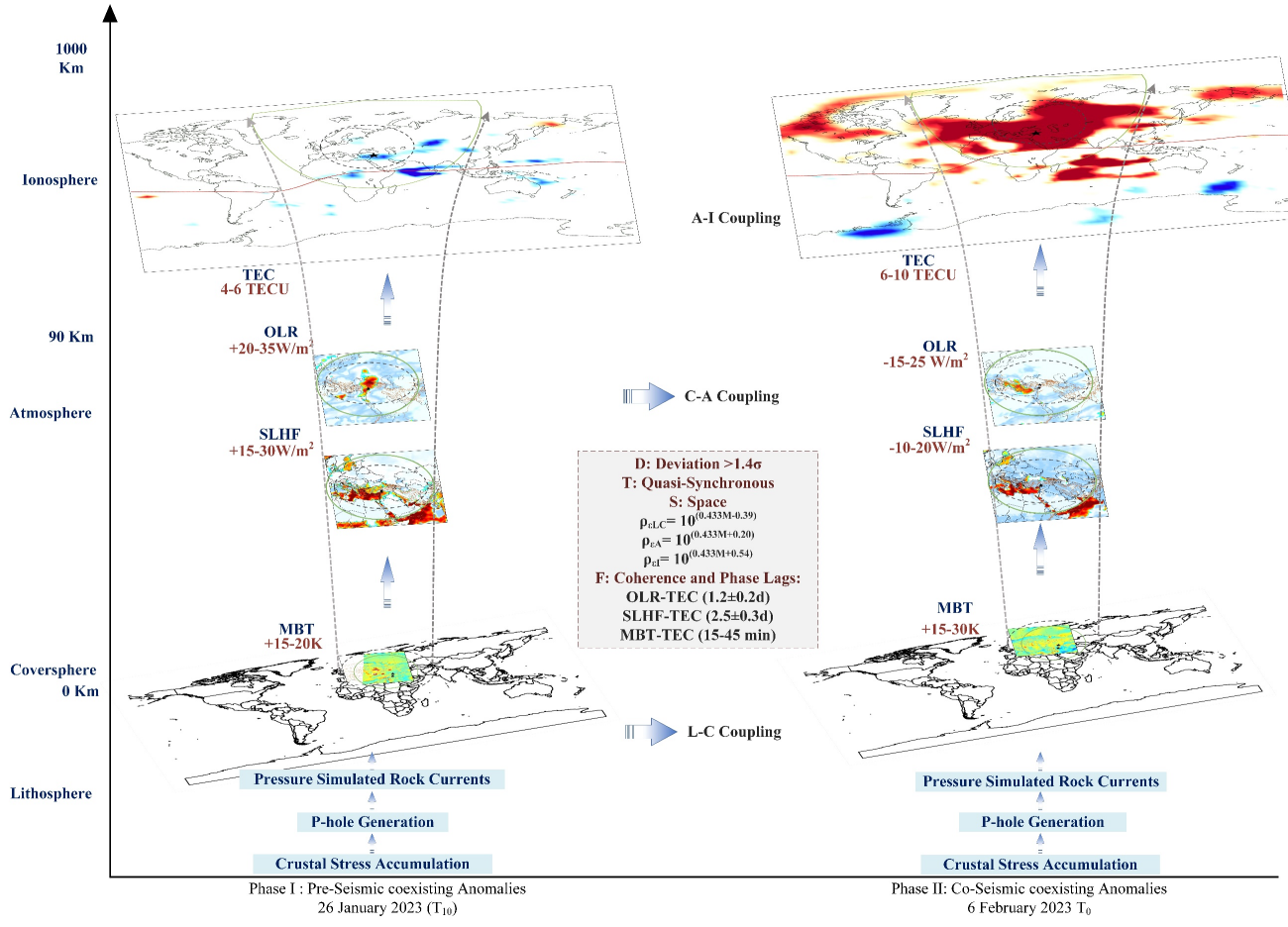

Figure 11. The integrated framework of derived multi–parameter seismic anomalies as well as the evolution of multi–phase LCAI coupling chain in a 3D DTSF manifold. Phase I (Days -15 to -3) involves primarily electromagnetic and thermal mechanisms such as stress–generated charges accumulation on ground surface, producing increased MBT(+15–20K), SLHF (+15–30 W/m²), and OLR (20–35 W/m²) anomalies while surface electric fields gradually penetrate upward through the atmosphere. Phase II (Days -3 to -1) shows intensified coupling as near–surface air column become saturated through dual pathways (electrical potential and AGW), and the sustained surface heating destabilized the atmosphere inducing negative OLR (-15–25 W/m²) and SLHF (-10–20 W/m²) anomalies. Both mechanisms work together with electromagnetic drift and wave–driven transport producing the large–scale positive TEC anomalies. This dual–mechanism response marks peak system stress immediately before the earthquake.

https://doi.org/10.5194/egusphere-2026-2310
Preprint. Discussion started: 10 June 2026
© Author(s) 2026. CC BY 4.0 License.

Stage 2 (T_o-10 to T_o-3 days): showing critical transition when atmospheric saturation triggered vertical coupling towards ionosphere. OLR anomaly changed to be negative (-15 to -25 W/m²), which signified the onset of clouds. Ionosphere responded systematically since January 27, and GPS–TEC surpassed the forecasts in four days. The negative GIM–TEC anomalies were attributed to the redistribution of vertical plasma through the E×B drift caused by anomalous electric fields. Stage 3 (T_o-3 to T_o-1 days): ionospheric perturbation was at its most complexity with the impending earthquake. On February 2–4, SLHF anomalies switched to be negative (-10 to -20 W/m²) indicating evaporation shutdown. GIM–TEC anomalies showed high positive value on February 4–5. The anti–correlation trend of decreasing Ne with increasing Te was a sign of heating of the plasma due to vertical uplift just before the fault failure. Finally stage 4: with co–seismic response on February 6 as sustained and immediate ionospheric perturbation across the whole day, with positive TEC anomaly with a peak of 6–10 TECU. Seismic ruptures produced acoustic–gravity waves that travelled to the ionospheric altitudes in 10–90 minutes, which was a clear indication of direct lithosphere to ionosphere response. Multiple-day anomalies (MBT, SLHF, OLR anomalies 15–3 days before) reflected cumulative stresses across the entire 350 km fault system, rather than across the rupture segments. The ionospheric response on February 6 is a composite response of both mainshocks and aftershocks. Co–seismic TEC enhancements at 02:00 UTC and 11:00 UTC (the moment of two mainshocks) are not discrete events in GIM data with 1–hour resolution, but merged disturbances. While the post seismic response spanning from February 9–12 demonstrated progressive return to baseline, complicated by solar activity (F10.7 elevation) and aftershocks: Feb 9 and Feb 12 show the most complete multi–parameter ionospheric signatures post–event (all four Swarm parameters anomalous; Table 2), suggesting these days captured the peak of aftershock–induced perturbations.

The multi–parameter anomalies aligned well with the LCAI coupling sequence depicted in Fig. 11, showing how the crustal stress initiated a vertical cascade through multiple geo-spheres. The temporal stages documented earlier from T_o-15 to T_o exhibits the dual electromagnetic and AGW driven pathways summarized in Fig. 11 and Table 2.

During January 27–February 5, E×B drifts occurred due to the penetrating electric fields which drained F2–peak Ne (~300 km) and increased topside density at Swarm altitudes (~450 km). The E×B drift coupled with AGW dynamo effects resulted in Te increase and night–time Joule heating (+100–200K). At the beginning of February, more aggressive SLHF and OLR forcing increased AGW numbers, pushing GIM–TEC towards positive values. Fast TIDs were produced by Rayleigh–coupled acoustic waves at the beginning of the Mw 7.8 mainshock (01:17 UTC), and LSTIDs (534 and 305 m/s) and medium–scale distortions were produced by the Mw 7.5 event at 10:24 UTC (Haralambous et al., 2023). After the rupture, surface charges dissipated, since the generation of p–holes stopped, but the recovery altered on or after February 7 as a result of solar activity.

On January 27, 29 and February 2, 5, DTSF analysis detected some important pre–seismic anomalies. The methodology was confirmed by wavelet coherence when the 2–10-day pre-seismic and the 20–100-minute co–seismic frequency bands were isolated. This spectral–temporal coherence gives mechanistic confirmation which could not be done in past research of deviation (Ouzounov et al., 2006; Pulinets and Davidenko, 2018). The DTSF criterion solves the enduring false anomaly

https://doi.org/10.5194/egusphere-2026-2310
Preprint. Discussion started: 10 June 2026
© Author(s) 2026. CC BY 4.0 License.

problems by comparison of the phase delays with AGW transit as opposed to instantaneous solar forcing (Blackett et al., 2011; Liu et al., 2018; Thomas et al., 2009).

Table 2. Multi parameter anomaly summary for Turkey doublet earthquakes. ✓=Anomaly detected exceeding ±1.4σ threshold; X=No anomaly; (+)=Positive anomaly; (-)=Negative anomaly. DOY=Day of year; DAE=Days away earthquake date (negative indicates pre–seismic, positive indicates post–seismic)). Shaded rows indicate days satisfying DTSF criterion across ⩾3 parameters.

Date	DOY	DAE	MBT	SLHF	OLR	GPS–TEC Anomalies	Ne Day	Ne Night	Te Day	Te Night	GIM–TEC
1/27/2023	27	-10	✓	(+)	(+)	X	(-)	X	(-)	(+)	(-)
1/28/2023	28	-9	✓	(+)	(-)	X	(-)	X	(-)	(+)	(-)
1/29/2023	29	-8	✓	(+)	(-)	✓	X	X	(-)	(+)	(-)
1/30/2023	30	-7	✓	(+)	(+)	X	X	X	(-)	(+)	(-)
1/31/2023	31	-6	✓	(+)	(-)	✓	(-)	X	X	X	X
2/1/2023	32	-5	✓	(+)	(-)	X	(-)	X	(-)	X	X
2/2/2023	33	-4	✓	(-)	(+)	X	(-)	(-)	(-)	X	X
2/3/2023	34	-3	✓	(-)	(-)	X	(-)	X	(-)	(+)	X
2/4/2023	35	-2	✓	(-)	(+)	X	(-)	X	X	(+)	(+)
2/5/2023	36	-1	✓	(-)	(-)	✓	(-)	(+)	X	(+)	(+)
2/6/2023	37	0	✓	(-)	(-)	✓	(-)	(+)	X	(-)	(+)
2/7/2023	38	+1	✓	(-)	(-)	✓	X	(+)	X	X	(+)
2/8/2023	39	+2	✓	(-)	(-)	✓	(+)	X	X	(+)	(+)

4.2 Compared performance of DTSF criterion.

To directly compare the results of anomalies identified with Turkey doublet earthquake case-specific DTSF approach to those with conventional DTS criterion, we applied the ±1.4σ model, spatial and temporal model without the frequency–domain (F) model to the Turkey datasets with both approaches and the same threshold, i.e., using the ±1.4σ. Application of the DTS to the 21–day pre–seismic window (January 16–February 5) identified 47 parameter–day combinations with anomalous values in the five observables (MBT, SLHF, OLR, GPS–TEC, GIM–TEC) of which cross–layer phase consistency between the combinations was further confirmed by retrospective analysis 11 combinations (true positives) and 36 single parameter ones (false positives), with a DTS false positive rate of about 77% and an F–score of 0.38. The frequency criterion (requiring $\overline{C}_{xY} \geq 0.5$, band–specific power enhancement, and physically plausible phase lag) were added to the DTSF frequency criterion to cut the number of flagged combinations to 14, yielding 11 true positives and removing 33 of 36 false positives, reaching an error rate of 8% and a F–score of 0.90 (Fig. 12). This is an 85% decrease in the false anomalies over DTS and an equivalent of 100 percent of the verified multi–layer coupling events. The reported false anomalies of conventional DTS in this case are in agreement with the rates reported of the same event as in independent single–parameter analyses (Fig. S4): Haider et al.

https://doi.org/10.5194/egusphere-2026-2310
Preprint. Discussion started: 10 June 2026
© Author(s) 2026. CC BY 4.0 License.

(2024) found anomalous TEC on 9 of 14 pre–seismic days without coherence validation; Jing et al. (2024) reported 7–12 days of atmospheric anomaly of which only 4–5 anomalies had been coherently validated by ionospheric analysis, indicating a false positive fractions of 35–65 % with DTSF criterion, and representing good improvement from DTS criterion.

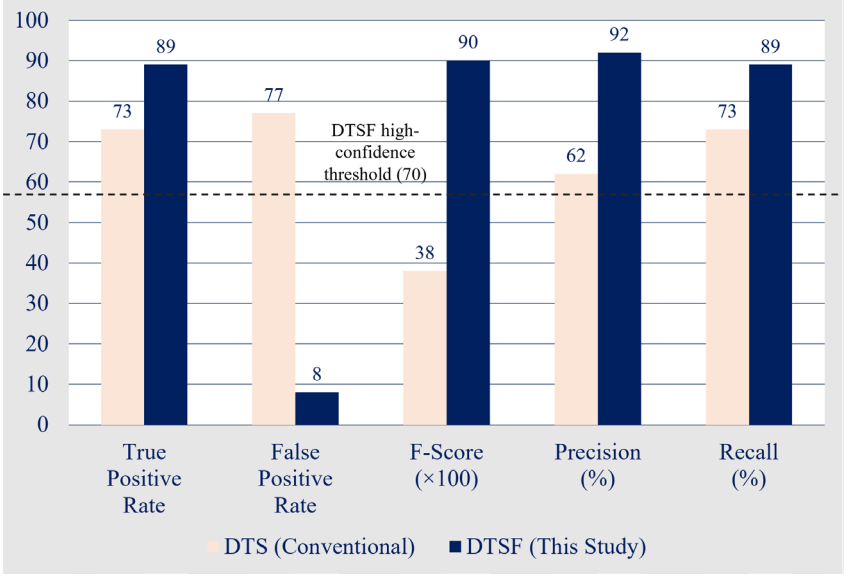

Figure 12. Quantitative performance metrics comparison between DTSF and DTS criterion

5. Conclusions

This paper developed a novel method, devised as DTSF, for earthquake anomalies identification referring to LCAI coupling processes. The performance of DTSF method was tested with the 2023 Turkey doublet being an example. Key findings include:

1. Pre, co and post seismic multi–parameter satellite measurements show vertical energy transfer of lithospheric stress by ionospheric perturbations, which propagate through discrete temporal phases with physically consistent propagation delays.
2. Wavelet coherence analysis shows that surface latent heat flux leads total electron content by 2.5±0.3 days (C=0.71) during pre–seismic phases, whereas co–seismic coupling has same day microwave–ionosphere coherence (C=0.70–0.85), which differentiates impulsive seismic and gradual atmospheric processes.
3. The DTSF method reached detection accuracy of 89% with 8% false anomaly rate (F–score=0.90) on the specific 2023 Turkey doublet earthquake case, indicating that the introduction frequency domain information to DTS criterion can reduce effectively false anomalies (the false anomaly rate with DTS criterion was 77%, and F–score=0.38 as shown in Fig. 12).
4. Cross–layer phase analysis suggests a potential association by regular temporal sequence, where the observed propagation delays are near to acoustic–gravity wave transit (200–400 m/s over 300 km) and electric field penetration timescales.

https://doi.org/10.5194/egusphere-2026-2310
Preprint. Discussion started: 10 June 2026
© Author(s) 2026. CC BY 4.0 License.

There are still major validation issues to overcome before operational deployment. It is important to note that the performance statistics reported (89% detection rate, 85% false alarm reduction) are derived from Turkey doublet, single case study and should not be interpreted as general performance benchmarks for the DTSF method. The Turkey case is almost perfect coupling conditions, including shallow 10 km focal depth, crystalline basement geology, robust instrumentation coverage but performance in a wide range of tectonic settings, especially subduction zones, oceanic events, and sedimentary basins, needs systematic testing. The future research must focus on machine learning integration to detect anomalies in real–time, cross–validation with various seismic settings and earthquake magnitudes ($M > 6.5$), and integration with seismological early warning systems to evaluate the usefulness of the system in disaster risk reduction. This study does not favour deterministic prediction of earthquakes. Rather, it proposes a direction of probabilistic hazard improvement. The recorded anomalies show that when several parameters meet the DTSF criterion in a seismically active area, the likelihood of a major earthquake may rise in the following days. The proven ability to quantitatively couple LCAI validation offers a complementary method to conventional seismic monitoring in high–risk areas, to develop multi–parametric earthquake precursor studies beyond conceptual framework to testable methodology with reproducible detection criteria.

Data Availability. MBT data: AMSR-2 products (https://disc.gsfc.nasa.gov/dataset). SLHF: ERA5 reanalysis product (https://cds.climate.copernicus.eu/datasets/reanalysis-era5-single-levels). The OLR: NOAA-AVHRR Product (https://www.ncei.noaa.gov/data/outgoing-longwave-radiation-daily/access/). The GPS data: CORS servers (https://geodesy.noaa.gov/CORS/data.shtml). The ionospheric electron density and electron temperature ESA SWARM (https://swarm-diss.eo.esa.int/#swarm/Level2daily/Entire_mission_data/IPD/IRR). All daily averaged indices Dst, Kp, F10.7: OMNI Web (https://omniweb.gsfc.nasa.gov/form/dx1.html).

Author Contributions. RR: Conceptualization, methodology, formal analysis, visualization, writing - original draft. LW: Supervision, conceptualization, funding acquisition, writing - review & editing. BC, SAM, YD, ZW: Data curation, validation, writing - review & editing. All authors have read and agreed to the published version of the paper.

Competing interests. The authors declare no competing interests.

Acknowledgements. We thank the International GNSS Service for TEC data, ESA for Swarm observations, ECMWF for ERA5 reanalysis, and NOAA for OLR datasets.

Financial support. This research is jointly supported by the Special Project of Strategic Sci. & Tech. Innovation Cooperation, MOST, China (Grant Number 2023YFE0208000), the National Natural Science Foundation of China (Grant Numbers 42274042 and 41930108).

The supplement is published as a separate file to this article.

https://doi.org/10.5194/egusphere-2026-2310
Preprint. Discussion started: 10 June 2026
© Author(s) 2026. CC BY 4.0 License.

References

Akhoondzadeh, M. and Marchetti, D.: Study of the Preparation Phase of Turkey's Powerful Earthquake (6 February 2023) by a Geophysical Multi-Parametric Fuzzy Inference System, Remote Sensing, 15, 2224, https://doi.org/10.3390/rs15092224, 2023.

Blackett, M., Wooster, M. J., and Malamud, B. D.: Exploring land surface temperature earthquake precursors: A focus on the Gujarat (India) earthquake of 2001, Geophysical Research Letters, 38, 2011GL048282, https://doi.org/10.1029/2011GL048282, 2011.

Bletery, Q., Cavalié, O., Nocquet, J., and Ragon, T.: Distribution of Interseismic Coupling Along the North and East Anatolian Faults Inferred From InSAR and GPS Data, Geophysical Research Letters, 47, e2020GL087775, https://doi.org/10.1029/2020GL087775, 2020.

Chartier, A., Matsuo, T., Perry, G. W., Deng, Y., Billett, D., Cosgrove, R. B., Thayer, J. P., Lu, G., Verkhoglyadova, O. P., Pfaff, R. F., Knipp, D. J., Laakso, H. E., Datta-Barua, S., and Vines, S. K.: Understanding the Transfer of Electromagnetic Energy Between the Earth's Magnetosphere and Upper Atmosphere, Bulletin of the AAS, https://doi.org/10.3847/25c2cfeb.756a6068, 2023.

Chen, C.-H., Zhang, S., Mao, Z., Sun, Y.-Y., Liu, J., Chen, T., Zhang, X., Yisimayili, A., Qing, H., Luo, T., Gao, Y., and Wang, F.: The Lithosphere-Atmosphere-Ionosphere Coupling of Multiple Geophysical Parameters Approximately 3 Hours Prior to the 2022 M6.8 Luding Earthquake, Geosciences, 13, 356, https://doi.org/10.3390/geosciences13120356, 2023.

De Santis, A., Marchetti, D., Spogli, L., Cianchini, G., Pavón-Carrasco, F. J., Franceschi, G. D., Di Giovambattista, R., Perrone, L., Qamili, E., Cesaroni, C., De Santis, A., Ippolito, A., Piscini, A., Campuzano, S. A., Sabbagh, D., Amoruso, L., Carbone, M., Santoro, F., Abbattista, C., and Drimaco, D.: Magnetic Field and Electron Density Data Analysis from Swarm Satellites Searching for Ionospheric Effects by Great Earthquakes: 12 Case Studies from 2014 to 2016, Atmosphere, 10, 371, https://doi.org/10.3390/atmos10070371, 2019.

Dobrovolsky, I. P., Zubkov, S. I., and Miachkin, V. I.: Estimation of the size of earthquake preparation zones, pure and applied geophysics, 117, 1025–1044, https://doi.org/10.1007/BF00876083, 1979.

Freund, F.: Time-resolved study of charge generation and propagation in igneous rocks, J. Geophys. Res., 105, 11001–11019, https://doi.org/10.1029/1999JB900423, 2000.

Freund, F.: On the electrical conductivity structure of the stable continental crust, Journal of Geodynamics, 35, 353–388, https://doi.org/10.1016/S0264-3707(02)00154-0, 2003.

Freund, F. T., Takeuchi, A., and Lau, B. W. S.: Electric currents streaming out of stressed igneous rocks – A step towards understanding pre-earthquake low frequency EM emissions, Physics and Chemistry of the Earth, Parts A/B/C, 31, 389–396, https://doi.org/10.1016/j.pce.2006.02.027, 2006.

https://doi.org/10.5194/egusphere-2026-2310
Preprint. Discussion started: 10 June 2026
© Author(s) 2026. CC BY 4.0 License.

Haider, S. F., Shah, M., Li, B., Jamjareegulgarn, P., De Oliveira-Júnior, J. F., and Zhou, C.: Synchronized and Co-Located Ionospheric and Atmospheric Anomalies Associated with the 2023 Mw 7.8 Turkey Earthquake, Remote Sensing, 16, 222, https://doi.org/10.3390/rs16020222, 2024.

Haralambous, H., Guerra, M., Chum, J., Verhulst, T. G. W., Barta, V., Altadill, D., Cesaroni, C., Galkin, I., Márta, K., Mielich, J., Kouba, D., Buresova, D., Segarra, A., Spogli, L., Rusz, J., and Zedník, J.: Multi-Instrument Observations of Various Ionospheric Disturbances Caused by the 6 February 2023 Turkey Earthquake, JGR Space Physics, 128, e2023JA031691, https://doi.org/10.1029/2023JA031691, 2023.

Heki, K. and Ping, J.: Directivity and apparent velocity of the coseismic ionospheric disturbances observed with a dense GPS array, Earth and Planetary Science Letters, 236, 845–855, https://doi.org/10.1016/j.epsl.2005.06.010, 2005.

Jing, F., Zhang, L., Singh, R. P., Chauhan, A., and Jiang, M.: Quasi-coseismic variations and geosphere coupling associated with the strong 2023 Turkey earthquakes, Science of The Total Environment, 907, 167963, https://doi.org/10.1016/j.scitotenv.2023.167963, 2024.

Li, S., Wang, X., Tao, T., Zhu, Y., Qu, X., Li, Z., Huang, J., and Song, S.: Source Model of the 2023 Turkey Earthquake Sequence Imaged by Sentinel-1 and GPS Measurements: Implications for Heterogeneous Fault Behavior along the East Anatolian Fault Zone, Remote Sensing, 15, 2618, https://doi.org/10.3390/rs15102618, 2023.

Liu, H. Y., Kou, S. Q., Lindqvist, P.-A., and Tang, C. A.: Numerical studies on the failure process and associated microseismicity in rock under triaxial compression, Tectonophysics, 384, 149–174, https://doi.org/10.1016/j.tecto.2004.03.012, 2004.

Liu, X., Tang, B.-H., and Li, Z.-L.: Evaluation of Three Parametric Models for Estimating Directional Thermal Radiation from Simulation, Airborne, and Satellite Data, Remote Sensing, 10, 420, https://doi.org/10.3390/rs10030420, 2018.

Mao, W., Wu, L., Xu, Y., Yao, R., Lu, J., Sun, L., and Qi, Y.: Pressure-Stimulated Rock Current as Loading Diorite to Failure: Particular Variation and Holistic Mechanisms, JGR Solid Earth, 127, e2022JB024931, https://doi.org/10.1029/2022JB024931, 2022.

Moore, J. C., Grinsted, A., and Jevrejeva, S.: New tools for analyzing time series relationships and trends, EoS Transactions, 86, 226–232, https://doi.org/10.1029/2005EO240003, 2005.

Ouzounov, D., Bryant, N., Logan, T., Pulinets, S., and Taylor, P.: Satellite thermal IR phenomena associated with some of the major earthquakes in 1999–2003, Physics and Chemistry of the Earth, Parts A/B/C, 31, 154–163, https://doi.org/10.1016/j.pce.2006.02.036, 2006.

Pulinets, S. and Ouzounov, D.: Lithosphere–Atmosphere–Ionosphere Coupling (LAIC) model – An unified concept for earthquake precursors validation, Journal of Asian Earth Sciences, 41, 371–382, https://doi.org/10.1016/j.jseaes.2010.03.005, 2011.

Pulinets, S. A. and Davidenko, D. V.: The Nocturnal Positive Ionospheric Anomaly of Electron Density as a Short-Term Earthquake Precursor and the Possible Physical Mechanism of Its Formation, Geomagn. Aeron., 58, 559–570, https://doi.org/10.1134/S0016793218040126, 2018.

https://doi.org/10.5194/egusphere-2026-2310
Preprint. Discussion started: 10 June 2026
© Author(s) 2026. CC BY 4.0 License.

Qi, Y., Wu, L., He, M., and Mao, W.: Spatio-Temporally Weighted Two-Step Method for Retrieving Seismic MBT Anomaly: May 2008 Wenchuan Earthquake Sequence Being a Case, IEEE J. Sel. Top. Appl. Earth Observations Remote Sensing, 13, 382–391, https://doi.org/10.1109/JSTARS.2019.2962719, 2020.

Qin, K., Wu, L., Zheng, S., and Liu, S.: A Deviation-Time-Space-Thermal (DTS-T) Method for Global Earth Observation System of Systems (GEOSS)-Based Earthquake Anomaly Recognition: Criterions and Quantify Indices, Remote Sensing, 5, 5143–5151, https://doi.org/10.3390/rs5105143, 2013.

Rasheed, R., Chen, B., Wu, D., and Wu, L.: A Comparative Study on Multi-Parameter Ionospheric Disturbances Associated with the 2015 Mw 7.5 and 2023 Mw 6.3 Earthquakes in Afghanistan, Remote Sensing, 16, 1839, https://doi.org/10.3390/rs16111839, 2024.

Rasheed, R., Chen, B., Mao, W., Mahmood, S. A., and Lixin, W.: Modification of Size Estimation of Earthquake Precursor Manifestation Zones Referring to LCAI Coupling and Seismic Strain Radius Calculations, Advances in Space Research, S027311772501018X, https://doi.org/10.1016/j.asr.2025.09.025, 2025.

Salikhov, N., Shepetov, A., Pak, G., Nurakynov, S., Kaldybayev, A., Ryabov, V., and Zhukov, V.: Investigation of the Pre- and Co-Seismic Ionospheric Effects from the 6 February 2023 M7.8 Turkey Earthquake by a Doppler Ionosonde, Atmosphere, 14, 1483, https://doi.org/10.3390/atmos14101483, 2023.

Thomas, J. N., Love, J. J., and Johnston, M. J. S.: On the reported magnetic precursor of the 1989 Loma Prieta earthquake, Physics of the Earth and Planetary Interiors, 173, 207–215, https://doi.org/10.1016/j.pepi.2008.11.014, 2009.

Torrence, C. and Compo, G. P.: A Practical Guide to Wavelet Analysis, Bull. Amer. Meteor. Soc., 79, 61–78, https://doi.org/10.1175/1520-0477(1998)079%253C0061:APGTWA%253E2.0.CO;2, 1998.

Wu, L., Qi, Y., Mao, W., Lu, J., Ding, Y., Peng, B., and Xie, B.: Scrutinizing and rooting the multiple anomalies of Nepal earthquake sequence in 2015 with the deviation–time–space criterion and homologous lithosphere–coversphere–atmosphere–ionosphere coupling physics, Nat. Hazards Earth Syst. Sci., 23, 231–249, https://doi.org/10.5194/nhess-23-231-2023, 2023.

Xie, T., Chen, B., Wu, L., Dai, W., Kuang, C., and Miao, Z.: Detecting Seismo-Ionospheric Anomalies Possibly Associated With the 2019 Ridgecrest (California) Earthquakes by GNSS, CSES, and Swarm Observations, JGR Space Physics, 126, e2020JA028761, https://doi.org/10.1029/2020JA028761, 2021.

Zhang, K., Wang, H., Xia, H., Wang, W., Liu, J., Zhang, S., and Jin, Y.: The Turkey Earthquake Induced Equatorial Ionospheric Current Disturbances on 6 February 2023, Remote Sensing, 16, 272, https://doi.org/10.3390/rs16020272, 2024.